

**Suprathermal electron acceleration by a quasi-perpendicular shock: simulations and observations**F.-J. KONG<sup>1</sup> AND G. QIN<sup>1</sup><sup>1</sup>*School of Science, Harbin Institute of Technology, Shenzhen, 518055, China; qingang@hit.edu.cn*

## ABSTRACT

The acceleration of suprathermal electrons in the solar wind is mainly associated with shocks driven by interplanetary coronal mass ejections (ICMEs). It is well known that the acceleration of electrons is much more efficient at quasi-perpendicular shocks than at quasi-parallel ones. Yang et al. (2018, ApJ, 853, 89) (hereafter YEA2018) studied the acceleration of suprathermal electrons at a quasi-perpendicular ICME-driven shock event to claim the important role of shock drift acceleration (SDA). Here, we perform test-particle simulations to study the acceleration of electrons in this event, by calculating the downstream electron intensity distribution for all energy channels assuming an initial distribution based on the averaged upstream intensities. We obtain simulation results similar to the observations from YEA2018 as follows. It is shown that the ratio of downstream to upstream intensities peaks at about 90° pitch angle. In addition, in each pitch angle direction the downstream electron energy spectral index is much larger than the theoretical index of diffusive shock acceleration. Furthermore, considering SDA, the estimated drift length is proportional to the electron energy but the drift time is almost energy independent. Finally, we use a theoretical model based on SDA to describe the drift length and time, especially, to explain their energy dependence. These results indicate the importance of SDA in the acceleration of electrons by quasi-perpendicular shocks.

## 1. INTRODUCTION

Shock acceleration is a crucial source for energetic particles in the heliosphere and galaxy. Charged particles gain energy via different mechanisms at shocks. The first one is first-order Fermi acceleration (FFA) due to the relative motion of scattering centers in the upstream and downstream regions. The second one is shock drift acceleration (SDA) as a result of gradient drift along the direction of convective electric field. The third one is stochastic acceleration (second-order Fermi) associated with the downstream turbulence. The well-known diffusive shock acceleration (DSA) theory (Axford et al. 1977; Krymsky 1977; Bell 1978; Blandford & Ostriker 1978), which successfully explains the power-law distribution of accelerated particles observed in the universe, is the combination of FFA and SDA.

Various heliospheric shocks, such as planetary bow shocks, coronal shocks, propagating interplanetary shocks, and the solar wind termination shock, are excellent acceleration sites of particles. It is assumed that there are two kinds of solar energetic particle (SEP) events observed at 1 au, one is impulsive events originating in solar flares (e.g., Cliver et al. 1982; Mason et al. 1984; Cane et al. 1986), the other is gradual events associated with interplanetary shocks driven by coronal mass ejections (CMEs) (e.g., Kahler et al. 1978, 1984; Reames 1999). Most space weather disturbances can be traced to large and long-duration gradual SEP events. Particle acceleration by CME-driven shocks has been widely studied (e.g., Reames et al. 1996; Zank et al. 2000; Li et al. 2003; Rice 2003; Desai & Burgess 2008; Kong et al. 2017, 2019; Qin et al. 2018); however, some problems still remain unresolved concerning particle acceleration at propagating interplanetary shocks. The geometry on the shock surface is variable when a CME-driven shock propagates from the sun into the interplanetary space. In addition, the turbulence level and other solar wind conditions are changeable. Therefore it is important to study the shock acceleration efficiency with varying obliquity angle, turbulence level, and other conditions (e.g., Giacalone 2005; Guo & Giacalone 2015; Qin et al. 2018). It is suggested by Qin et al. (2018) that particle acceleration processes with weak scatterings (weak turbulence) are generally FFA for parallel (quasi-parallel) shocks and SDA for perpendicular (quasi-perpendicular) shocks, and that SDA is more efficient than FFA.

Recently, some interesting phenomena are observed in the acceleration of electrons by shocks. On the one hand, energetic electrons can be produced by shock acceleration near the sun. Holman & Pesses (1983) sug-

gested that electrons are accelerated to high energies in the solar corona by SDA. Energetic electrons, which are observed as solar type II radio bursts, can also be generated via resonant interaction with whistler waves at quasi-perpendicular shocks in the solar corona (Miteva & Mann 2007). Furthermore, Li et al. (2013) and Kong et al. (2013) studied electron spectral hardening in solar flares with observations from Gamma-Ray Spectrometer (SMM) onboard *Solar Maximum Mission (SMM)*, to suggest that energetic electrons are produced by SDA.

On the other hand, there exists low-energy electrons in interplanetary (IP) space such as suprathermal electrons, which, to constitute important components of solar wind halo, strahl, and superhalo populations (e.g., Feldman et al. 1975; Lin 1998; Maksimovic et al. 2005), can be accelerated by following the meandering magnetic field lines repeatedly across the shock (Jokipii & Giacalone 2007; Guo & Giacalone 2010). Kajdič et al. (2014) found 90° pitch angle enhancements of suprathermal electrons at IP shocks measured by Solar Wind Electron Analyzer (SWEA) onboard *STEREO-A*. Yang et al. (2018, hereafter YEA2018) investigated two strong electron flux enhancement events measured by electron electrostatic analyzers (EESA) in the 3DP instrument onboard *Wind*, one with a quasi-perpendicular shock, the other one with a quasi-parallel shock. It is found that at energies of  $\sim 0.4\text{--}50$  keV, the ratios of the downstream to ambient electron intensities all peak at around 90° pitch angle. Besides, the energy spectrum in each pitch angle direction in the downstream can be fit to a double power-law with a spectral index much larger than the theoretical one from DSA. They thus assumed that SDA is the dominant acceleration mechanism in both the shock events, and they obtained that the drift length is roughly proportional to the electron energy but the drift time almost does not vary with energy.

In Kong & Qin (2019) we performed numerical simulations to obtain 90° pitch angle enhancements for three sample energy channels in the range of 89–257 eV at a quasi-perpendicular shock on 24 April 2008 that was studied by Kajdič et al. (2014). In this paper, we study numerically the acceleration of suprathermal electrons in the range of  $\sim 0.3\text{--}40$  keV at the quasi-perpendicular shock on 2000 February 11 that was studied by YEA2018. Pitch angle distributions (PADs) for all of the 12 energy channels, energy spectra for the parallel, perpendicular, and anti-parallel directions, and spectral indices for all pitch angles are obtained by solving the motion equation of electrons using a backward-in-time test-particle method. The electron

drift length and drift time are also estimated using the method of unchanged phase space density after the acceleration of electrons (YEA2018). Finally, a theoretical model is obtained to describe the drift length and drift time. In Section 2 we briefly introduce the instruments onboard *Wind* used in the study, and we list the shock parameters for the event. We describe our physical and numerical models to accelerate electrons in Section 3. In Section 4, we first show the estimation of electron drift length and drift time from the data of distribution functions following YEA2008, then we provide a theoretical model of drift length and drift time. In Section 5 the simulation results and comparisons with observations are presented. Finally, we show in Section 6 the discussion and conclusions.

## 2. OBSERVATIONS

The *Wind* spacecraft was launched on November 1, 1994, and located around the L1 Lagrangian point. The 3DP instrument onboard *Wind* is designed to measure the distribution of suprathermal electrons and ions in the solar wind. The electron electrostatic analyzers (EESA) in the 3DP instrument measures the energy ranges of  $\sim 3\text{--}1000$  eV and  $\sim 0.1\text{--}30$  keV, respectively, for the low and high energy detectors. The 3DP instrument provides three-dimensional data with eight pitch angle channels of  $22.5^\circ$  interval. For more details of *Wind* 3DP instrument see [Lin et al. \(1995\)](#). The magnetic field data are measured by the magnetic field instrument (MFI) (see, [Farrell et al. 1995](#)), and the plasma parameters in the solar wind such as bulk flow speed  $V_{\text{sw}}$  and proton number density  $n_p$  are provided by the Solar Wind Experiment (SWE) instrument ([Ogilvie et al. 1995](#)).

As already mentioned above, we focus on the acceleration of electrons by the quasi-perpendicular shock on 2000 February 11. The shock arrived at *Wind* at 23:34 UT according to *Wind* IP shock list [https://www.cfa.harvard.edu/shocks/wi\\_data/](https://www.cfa.harvard.edu/shocks/wi_data/), with a shock-normal angle of  $\theta_{\text{Bn}} \sim 89^\circ$ , a shock speed of  $V_{\text{sh}} \sim 682$  km s $^{-1}$ , and a compression ratio  $s \sim 2.87$  from calculations of YEA2018. The upstream magnetic field, solar wind bulk speed, and proton number density are set to be  $B_{01} = 7.0$  nT,  $V_{\text{sw}} = 434$  km s $^{-1}$ , and  $n_p = 5.19$  cm $^{-3}$ , respectively, by averaging the observational data over the time range of 23:20–23:30 (data used from the website <https://cdaweb.sci.gsfc.nasa.gov>). The upstream speed is set to be  $U_1 = V_{\text{sh}} - V_{\text{sw}} \sim 248$  km s $^{-1}$  for simplicity. We obtain the upstream Alfvén speed  $V_{\text{A1}} = 67$  km s $^{-1}$ , and Alfvén Mach number  $M_{\text{A1}} = 3.70$ .

### 3. IP SHOCK MODELS TO ACCELERATE ELECTRONS

We study here the acceleration of electrons at an IP shock by solving numerically the equation of motion of test particles, and such method has been used in previous studies (Decker & Vlahos 1986a,b; Giacalone 2005; Giacalone & Jokipii 2009; Kong et al. 2017, 2019; Qin et al. 2018).

#### 3.1. Physical Model

For simplicity, we consider a planar shock with the geometry shown in the cartoon of Figure 1 in Kong et al. (2017). The shock is located at  $z = 0$  with a thickness  $L_{\text{th}}$ . The plasma flows in the positive  $z$ -direction with the upstream and downstream speeds,  $U_1$ ,  $U_2$ , respectively, in the shock frame. In this work, we usually use subscripts 1 and 2 to indicate the upstream and downstream, respectively. In the shock transition the plasma speed is assumed to be in the form of

$$U(z) = \frac{U_1}{2s} \left\{ (s+1) + (s-1) \tanh \left[ \tan \left( -\frac{\pi z}{L_{\text{th}}} \right) \right] \right\}, \quad (1)$$

where  $s$  is the shock compression ratio. The motion equation of test particles is given by

$$\frac{d\mathbf{p}}{dt} = q[\mathbf{E}(\mathbf{r}, t) + \mathbf{v} \times \mathbf{B}(\mathbf{r}, t)], \quad (2)$$

where  $\mathbf{p}$  is the particle momentum,  $\mathbf{v}$  is the particle velocity,  $q$  is the electron charge,  $t$  is time. The electric field  $\mathbf{E}$  is the convective electric field  $\mathbf{E} = -\mathbf{U} \times \mathbf{B}$ . The total magnetic field consists of the background magnetic field and turbulent magnetic field, and is given by

$$\mathbf{B}(x', y', z') = \mathbf{B}_0 + \mathbf{b}(x', y', z'). \quad (3)$$

Note that the background magnetic field  $\mathbf{B}_0$  is in the  $x - z$  plane. The input parameters for the shock are shown in Table 1. The value of shock thickness  $L_{\text{th}}$  is set as  $2 \times 10^{-6}$  au according to YEA2018.

The turbulent magnetic field is given by

$$\mathbf{b}(x', y', z') = \mathbf{b}_{\text{slab}}(z') + \mathbf{b}_{\text{2D}}(x', y'), \quad (4)$$

where  $\mathbf{b}$  is a turbulent magnetic field perpendicular to  $\mathbf{B}_0$  with zero mean, and  $(x', y', z')$  is the coordinate system with  $z'$  in the direction of  $\mathbf{B}_0$ . The turbulent magnetic field  $\mathbf{b}$  is composed of slab and two-dimensional

(2D) components with the energy density ratio assumed to be  $E_{\text{slab}} : E_{2\text{D}} = 20 : 80$  (“two-component” model, Matthaeus et al. 1990; Zank & Matthaeus 1992; Bieber et al. 1996; Gray et al. 1996; Zank et al. 2006). We assume the slab correlation length  $\lambda = 0.02$  au at 1 au, and the 2D correlation length  $\lambda_x = \lambda/2.6$  on the basis of previous studies (Osman & Horbury 2007; Weygand et al. 2009, 2011; Dosch et al. 2013). A dissipation range in which low-energy electrons resonate is included in the slab turbulence, as applied in the work of Qin et al. (2018). The break wavenumber  $k_b$  from the inertial range to the dissipation range is assumed to  $k_b = 10^{-6} \text{ m}^{-1}$  based on the observational investigations in Leamon et al. (1999). The values of spectral indices of the inertial and dissipation ranges ( $\beta_i = 5/3$ ,  $\beta_d = 2.7$ ) are set as the same as those in Qin et al. (2018). A periodic turbulence box with sizes  $10\lambda \times 10\lambda$  and  $25\lambda$  for the 2D and slab components, respectively, is adopted in the simulations. The turbulence levels of the upstream and downstream regions are taken to be  $(b/B_0)^2 = 0.25$  and  $0.36$ , respectively. The input parameters for the turbulence are shown in Table 2.

### 3.2. Numerical Model

Based on the *Wind*/3DP observations, we simulate pitch angle distributions (PADs) of 12 energy channels with central energies  $\sim 0.266, 0.428, 0.691, 1.116, 1.952, 2.849, 4.161, 6.076, 8.875, 12.96, 27.32,$  and  $39.50$  keV. A backward-in-time test-particle method is used to simulate the PAD of a given energy channel  $E_i$  ( $i = 1, 2, 3, \dots, 12$ ) in the downstream of the shock. A total number of 30,000 electrons with an energy  $E_i$  and a pitch angle  $\mu_j$  are put into the downstream range  $[z_0, z_1]$  at the initial time  $t = 0$ , where  $z_0 = L_{\text{th}}$  and  $z_1 = V_{\text{sh}}\Delta t \approx 2.7 \times 10^{-3}$  au with  $\Delta t = 10$  min. We take the spatial domain size in the  $x, y, z$  directions to  $x_{\text{box}} = y_{\text{box}} = 10^4\lambda$  and  $z_{\text{box}} = 10^3\lambda$ . The trajectory of each electron is followed using an adaptive step fourth-order Runge-Kutta method with a normalized accuracy to  $10^{-9}$  until the simulation time  $t_{\text{acc}} = 10$  min. After the numerical calculations, a few electrons whose energy is less than  $0.1E_i$  are discarded. The downstream pitch angle distribution,  $f_{\text{dn}}(E_i, \mu_j)$ , for  $E_i$  channel can be obtained as

$$f_{\text{dn}}(E_i, \mu_j) = \frac{1}{N_{ij}} \sum_{k=1}^{N_{ij}} f_0(E_{ik}, \mu_{jk}), \quad (5)$$

where  $N_{ij}$  is the number of test particles in the statistics,  $f_0(E_{ik}, \mu_{jk})$  is the initial distribution, and  $E_{ik}$  and  $\mu_{jk}$  are the  $k$ th particle energy and pitch angle, respectively, when it is traced back to the initial time. The initial

distribution is constructed by averaging the 3DP data in the time period of 23:20–23:30 before the shock arrival. Note that we employ linear interpolation in log-log space between the adjacent particle energies to calculate the value of  $f_0(E_{ik}, \mu_{jk})$ . In addition, in this work, to use test-particle method, we do not consider wave excitation by the accelerated particles.

#### 4. DRIFT LENGTH AND TIME

##### 4.1. Estimation of electron drift length and time from distribution functions

In this subsection, following YEA2008, we show the estimation of the electron drift length and drift time. To consider SDA, according to Liouville's theorem, it is assumed that electrons remain the same phase space density after they are accelerated from the upstream to downstream, i.e.,

$$f_2(p_2) = f_1(p_1), \quad (6)$$

where  $p$  and  $f$  are the electron momentum and phase space density, respectively. Here, the subscripts 1 and 2 mean the upstream and downstream of the shock, respectively. The energy gain  $\Delta E$  after the acceleration of upstream electrons with a momentum  $p_1$  can be obtained considering the same phase space density. The electron drift length is then written as

$$L_{\text{drift}} = \frac{\Delta E}{q|E|}, \quad (7)$$

where  $E$  is the convection electric field.

According to Jokipii (1982), the gradient drift velocity at the shock front is

$$\mathbf{V}_{\text{drift}} = \hat{\mathbf{e}}_y \frac{pv}{3q} \left( \frac{B_{x1}}{B_1^2} - \frac{B_{x2}}{B_2^2} \right) \delta(z), \quad (8)$$

where  $B_1$  and  $B_2$  are the background magnetic fields with their  $x$ -components  $B_{x1}$  and  $B_{x2}$  in the upstream and downstream, respectively. We can integrate the above equation for  $z$  from  $-L_{\text{th}}/2$  to  $L_{\text{th}}/2$  to obtain the average gradient drift velocity

$$\bar{\mathbf{V}}_{\text{drift}} = \hat{\mathbf{e}}_y \frac{pv}{3qL_{\text{th}}} \left( \frac{B_{x1}}{B_1^2} - \frac{B_{x2}}{B_2^2} \right). \quad (9)$$

In addition, the drift time,  $T_{\text{drift}}$ , can be obtained by

$$T_{\text{drift}} = \frac{L_{\text{drift}}}{\bar{V}_{\text{drift}}}. \quad (10)$$

#### 4.2. A theoretical model for electron drift length and time

Next, we provide a theoretical model based on shock drift acceleration to describe the drift length and drift time. Since the electron gyroradius is much smaller than the shock thickness  $L_{\text{th}}$ , it is assumed that an electron can be accelerated by SDA when it is in the quasi-perpendicular shock transition range. On the other hand, when particles are in the shock transition range they would move the downstream as the fluid convection, so the electron drift time  $T_{\text{drift}}$  can be written as

$$T_{\text{drift}} = \frac{L_{\text{th}}}{2U_1} + \frac{L_{\text{th}}}{2U_2}, \quad (11)$$

where  $U_i$  indicates the fluid speed upstream and downstream of the shock with  $i = 1$  and  $i = 2$ , respectively. Since the shock thickness  $L_{\text{th}}$  and fluid convection speed  $U_i$  can be considered constant, the drift time  $T_{\text{drift}}$  is constant too,

$$T_{\text{drift}} \propto E^0. \quad (12)$$

Furthermore, according to Equations (9), (10), and (11), the electron drift length  $L_{\text{drift}}$  can be calculated as

$$L_{\text{drift}} = T_{\text{drift}} \bar{V}_{\text{drift}} = \frac{pv}{6q} \left( \frac{1}{U_1} + \frac{1}{U_2} \right) \left( \frac{B_{x1}}{B_1^2} - \frac{B_{x2}}{B_2^2} \right). \quad (13)$$

It is found that the electron drift length  $L_{\text{drift}}$  is proportional to  $E$  if the relativistic effects are not considered, i.e.,

$$L_{\text{drift}} \propto E. \quad (14)$$

## 5. SIMULATION RESULTS AND THE COMPARISONS WITH OBSERVATIONS

In Figure 1 we show the electron intensity versus pitch angle in the energy channels ranging from 0.266 to 39.50 keV for the shock event on 2000 Feb 11. As shown in the following, from observational data we get similar results as YEA2018 did. We also carry out a large scale numerical simulations for electron acceleration under the condition set for the event with the upstream observations as the initial distribution.

In the upper pannels of Figures 1(a)–(l), the blue and red diamonds show the 10-minute averaged observational data upstream and downstream of the shock, respectively, and the black circles show the downstream simulation results. It is shown that, except for the highest energy channel shown in Figure 1(l), the upstream



electron intensities display an anisotropic distribution with higher values in the parallel and anti-parallel magnetic field directions and lower values in the perpendicular direction. The anisotropy decreases as the energy increases. In Figure 1(l) with the highest energy, 39.50 keV, the observed upstream intensities are high and low in the parallel and anti-parallel directions, respectively, and the dramatic change of values happens around  $90^\circ$  pitch angle. The downstream simulation results indicate that electron intensities increase around  $\sim 90^\circ$  compared with upstream intensities.

In the lower pannels of Figures 1(a)–(l), red diamonds show the ratio of the downstream to upstream intensities for observations. It is shown that from observations for energy channels except for the largest energy one, the ratio in perpendicular directions is the largest. In the lower pannels of Figures 1(a)–(l) black circles show the ratio of downstream simulation intensities to upstream observation intensities. The lower panels of Figure 1 show that at all energy channels the ratio of the downstream to upstream electron intensities for both observations and simulations peaks at  $\sim 80^\circ$ – $100^\circ$ , with a much clear trend in the lower energy channels of 0.266–4.161 keV in Figure 1(a)–(g). This indicates that at quasi-perpendicular shocks there is the strongest acceleration in the pitch angle around  $90^\circ$ . In addition, this acceleration is more efficient for particles with lower energies.

For each pitch angle direction the integral energy intensities  $I_U$  and  $I_D$  in the upstream and downstream, respectively, are obtained by integrating the differential intensity over the energy range of 0.266–39.50 keV. In the upper panel of Figure 2, blue and red diamonds show the upstream and downstream observational integral energy intensities, respectively, and black circles indicate the downstream one from simulations. From the figure it is shown that, with observations, the upstream integral energy intensity has the lowest value in around  $90^\circ$  pitch angle. However, the downstream integral energy intensity is the highest in around  $90^\circ$  pitch angle, and relatively higher in the anti-parallel direction than in the parallel direction. In addition, the downstream integral energy intensity obtained from simulations, compared with the upstream integral energy intensity, is higher in around  $90^\circ$  pitch angle and lower in the parallel and anti-parallel directions. The lower panel of Figure 2 shows the ratio of the downstream to upstream integral energy intensities. It is shown that from both the observations (red diamonds) and simulations (black circles) the ratio reaches its peak around the perpendicular direction. This indicates that the shock acceleration efficiency is the strongest

in the perpendicular direction according to the observations and simulations. On the other hand, we can find that the ratio from observations is larger than that from simulations in the perpendicular direction, which indicates that our simulations do not produce shock acceleration efficiency as strong as that from observations. Furthermore, in the anti-parallel direction, the ratio from observations is larger than that from simulations. The reason might be that there are anisotropic beams in the anti-sunward-traveling (anti-parallel) direction in the downstream of the shock (YEA2018).

In Figure 3 we compare the energy spectra of electrons in the directions parallel (a), perpendicular (b), and anti-parallel (c) to the magnetic field. The blue and red diamonds denote 10-minute averaged electron intensities in the upstream and downstream of the shock, respectively. The black circles indicate the simulation results in the downstream. From the figure we can see that the observed downstream intensities are several times the upstream intensities in the perpendicular and anti-parallel directions, but they are similar in the parallel direction. In addition, the simulated downstream intensities increase significantly relative to the initial upstream intensities, which is set as the upstream observations, in the perpendicular direction, but they stay almost unchanged in the parallel and anti-parallel directions. It is shown that a more prominent intensity enhancement occurs in the perpendicular direction for both observations and simulations, especially in the energy channel of 0.266 keV the perpendicular intensity increases  $\sim 30$  times for observations and  $\sim 5$  times for simulations. We fit the electron spectrum in each direction as a power law with spectral indices  $\alpha_{1,o}$ ,  $\alpha_{2,o}$ , and  $\alpha_{2,s}$ , where subscripts 1 and 2 denote upstream and downstream, and o and s denote observations and simulations, respectively. The dashed line indicates the power-law fitting of the simulation results in the downstream. We can see that the values of  $\alpha_{1,o}$ ,  $\alpha_{2,o}$ , and  $\alpha_{2,s}$  are larger than  $\alpha_t = 1.30$  which is predicted by diffusive shock acceleration. It is shown that the direction perpendicular to the magnetic field at the quasi-perpendicular shock front plays an important role in the shock acceleration of particles.

In addition, we plot the energy spectral index as a function of electron pitch angle in Figure 4. Blue and red diamonds show the results from the upstream and downstream observations, respectively. We also show the spectral indices in the downstream from simulations with black circles. It is shown that the downstream spectral indices in the perpendicular direction from both observations and simulations are larger than the upstream one. It is assumed that there is more effective shock acceleration for lower energy par-

ticles, and strong shock acceleration causes much higher flux enhancement in the lower energy range for energetic particles, generating softer downstream particle spectrum. Accordingly, the much softer downstream energy spectrum from both observations and simulations relative to the upstream observations in the quasi-perpendicular direction indicates stronger shock acceleration in this direction. However, the observed spectral indices in the downstream are higher than those in the upstream in the anti-parallel direction, the reason might also be the anti-sunward-travelling beams downstream of the shock as mentioned above.

The fact that the acceleration of electrons in the perpendicular direction is more efficient reveals the importance of SDA process at quasi-perpendicular shocks. So that we calculate the electron drift length and drift time from the data of distribution functions using the method in YEA2018. As shown in Figure 5, the distribution functions,  $f_1$  (blue dashed line) and  $f_2$  (black dashed line), are obtained by a linear fit in log-log space to the data points from observations in the upstream (blue diamonds) and simulations in the downstream (black circles), respectively. We are able to obtain the energy gain  $\Delta E$  after the acceleration of upstream electrons with a momentum  $p_1$  with Equation (6), considering the same phase space density. It is noted that in this method, the data of distribution functions are used. Then, the electron drift length and drift time from simulations can be obtained through Equation (7) and Equation (10).

Figures 6(a) and (b) show the electron drift length  $L_{\text{drift}}$  and drift time  $T_{\text{drift}}$  as a function of energy, respectively. In Figure 6, red diamonds and black circles indicate results for observations from YEA2018 and simulations in this work, respectively. It is shown in Figure 6(a) that for the estimated result obtained from simulations the drift length increases linearly with the electron energy in log-log space with a slope  $\sim 1.1$ , which compares well with that from the observations with a slope  $\sim 1.0$ . In Figure 6(b), the linear fitting of the estimated drift time from simulations and electron energy in log-log space with a slope 0.14, also agrees approximately with that from the observations with a slope 0.00. In other words, the drift time almost does not vary with the energy according to both observations and simulations. We note that for the same energy channel the estimated drift length and drift time obtained from simulations in this work are lower than that from observations in YEA2018, which may due to the less efficient acceleration of electrons in our numerical model.

In addition, we use Equations (13) and (11) to calculate the theoretical results of electron drift length  $L_{\text{drift}}$  and drift time  $T_{\text{drift}}$ , respectively. With the theories, it is found that the electron drift length is proportional to energy  $E$  and the electron drift time is independent of energy. This is consistent with the observations and simulations shown in Figure 6(a) and (b). In Figure 6(a) and (b), blue dashed lines indicate the theoretical results of  $L_{\text{drift}}$  and  $T_{\text{drift}}$  from Equations (13) and (11), respectively. We can see that the theoretical results agree well with the observational ones, but they are several times larger than the simulation ones. The reason of the discrepancy might be that less efficient acceleration is achieved in our simulations.

## 6. DISCUSSION AND CONCLUSIONS

We have used test-particle numerical simulations of a backward-in-time test-particle method to study the acceleration of suprathermal electrons in the energy range of  $\sim 0.3\text{--}40$  keV at a quasi-perpendicular shock event on 2000 February 11 to compare with the observational study in YEA2018. We obtain electron pitch angle distributions from simulations for all 12 energy channels, and find that the ratio of the downstream to upstream differential intensities peaks at about  $\sim 90^\circ$  pitch angle. These results are in good agreement with the spacecraft observations in YEA2018. In addition, it is found that the observed and simulated electron energy spectral index for each pitch angle direction in the downstream is significantly larger than the theoretical index of diffusive shock acceleration. The results indicate that shock drift acceleration plays an important role in the acceleration of electrons at quasi-perpendicular shocks as suggested by YEA2018.

Furthermore, with Liouville's theorem, considering SDA, YEA2018 used observational data to show that the electron drift length  $L_{\text{drift}}$  is approximately proportional to the electron energy  $E$ . In addition, it is suggested that the drift time  $T_{\text{drift}}$  is almost independent of the electron energy. From our simulations we obtain the similar energy dependence of the drift length and drift time, but with values several times lower than those from the observations. Next, we provide theoretical models based on shock drift acceleration to describe the electron drift length and drift time, which agree well with the observational results. In addition, the theories can be used to explain the energy dependence of electron drift length and drift time found by observations and simulations.

It is suggested that the difference between the results from the observations and simulations show that our numerical model does not provide shock acceleration as effective as the observations. In addition, there

is anti-sunward-travelling beams of energetic electrons downstream of the shock in the observations which does not appear in our shock acceleration model.

### ACKNOWLEDGMENTS

This work was supported, in part, under grants NNSFC 41874206 and NNSFC 41574172. The work was carried out at National Supercomputer Center in Tianjin, and the calculations were performed on TianHe-1 (A). We gratefully acknowledge Dr. Linghua Wang for useful discussions about this topic.

### REFERENCES

- Axford, W. I., Leer, E., & Skadron, G. 1977, Proc. ICRC (Plovdiv), 11, 132
- Bell, A. R. 1978, MNRAS, 182, 147
- Bieber, J. W., Wanner, W., & Matthaeus, W. H. 1996, J. Geophys. Res., 101, 2511
- Blandford, R. D., & Ostriker, J. P. 1978, ApJL, 221, L29
- Cane, H. V., McGuire, R. E., von Rosenvinge, T. T. 1986, ApJ, 301, 448
- Cliver, E. W., Kahler, S. W., Shea, M. A., & Smart, D. F. 1982, ApJ, 260, 362
- Decker, R. B., & Vlahos, L. 1986a, ApJ, 306, 710
- Decker, R. B., & Vlahos, L. 1986b, J. Geophys. Res., 91, 13349
- Desai, M. I., & Burgess, D. 2008, J. Geophys. Res., 113, A00B06
- Dosch, A., Adhikari, L., & Zank, G. P. 2013, in 13th Int. Solar Wind Conf. (Solar Wind 13), 1539, 155
- Farrell, W. M., Thompson, R. F., Lepping, R. P., & Byrnes, J. B. 1995, IEEE Trans. on Magnetics, 31, 966
- Feldman, W. C., Asbridge, J. R., Bame, S. J., Montgomery, M. D., & Gary, S. P. 1975, J. Geophys. Res., 80, 31
- Giacalone, J. 2005, ApJ, 624, 765
- Giacalone, J., & Jokipii, J. R. ApJ, 701, 1865
- Gray, P. C., Pontius, D. H., Jr., & Matthaeus, W. H. 1996, Geophys. Res. Lett., 23, 965
- Guo, F., & Giacalone, J. 2010, ApJ, 715, 406
- Guo, F., & Giacalone, J. 2015, ApJ, 802, 97
- Holman, G., & Pesses, M. E. 1983, ApJ, 267, 837
- Jokipii, J. R. 1982, ApJ, 255, 716
- Jokipii, J. R., & Giacalone, J. 2007, ApJ, 660, 336
- Kahler, S. W., Hildner, W. E., & Van Hollebeke, M. A. I. 1978, SoPh, 57, 429
- Kahler, S. W., Sheeley Jr., N. R., Howard, R. A., et al. 1984, J. Geophys. Res., 89, 9683
- Kajdič P., Lavraud B., Zaslavsky A., et al. 2014, J. Geophys. Res.: Space Physics, 119, 7038
- Kong, F. J., & Qin, G. 2019, Chin. J. Space Sci., 39, 143
- Kong, F. J., Qin, G., Wu, S. S., Zhang, L. H., Wang, H. N., Chen, T., & Sun, P. 2019, ApJ, 877, 97

- Kong, F. J., Qin, G., & Zhang, L. H. 2017, *ApJ*, 845, 43
- Kong, X., Li, G., & Chen, Y. 2013, *ApJ*, 774, 140
- Krymsky, G. F. 1977, *DoSSR*, 234, 1306
- Leamon, R. J., Smith, C. W., Ness, N. F., & Wong, H. K. 1999, *J. Geophys. Res.*, 104, 22331
- Li, G., Zank, G. P., & Rice, W. K. M. 2003, *J. Geophys. Res.*, 108, 1082
- Li, G., Zank, G. P., & Chen, Y. 2013, *ApJ*, 769, 22
- Lin, R. P. 1998, *SSRv*, 86, 61
- Lin, R. P., Anderson, K. A., Ashford, S., et al. 1995, *SSRv*, 71, 125
- Maksimovic, M., Zouganelis, I., Chaufray, J. Y., et al. 2005, *J. Geophys. Res.*, 110, A09104
- Mason, G. M., Gloeckler, G., & Hovestadt, D. 1984, *ApJ*, 280, 902
- Matthaeus, W. H., Goldstein, M. L., & Roberts, D. A. 1990, *J. Geophys. Res.*, 95, 20673
- Miteva, R., & Mann, G. 2007, *A&A*, 474, 617
- Ogilvie, K. W., Chornay, D. J., Fritzenreiter, R. J., et al. 1995, *SSRv*, 71, 55
- Osman, K. T., & Horbury, T. S. 2007, *ApJL*, 654, L103
- Potter, D. W. 1981, *J. Geophys. Res.*, 86, 11111
- Qin, G., Kong, F. J., & Zhang, L. H. 2018, *ApJ*, 860, 3
- Reames, D. V., Barbier, L. M., & Ng, C. K. 1996, *ApJ*, 466, 473
- Reames, D. V. 1999, *SSRv*, 90, 413
- Rice, W. K. M., Zank, G. P., & Li, G. 2003, *J. Geophys. Res.*, 108, 1369
- Riquelme, M. A., & Spitkovsky, A. 2011, *ApJ*, 733, 63
- Weygand, J. M., Matthaeus, W. H., Dasso, S., et al. 2009, *J. Geophys. Res.*, 114, A07213
- Weygand, J. M., Matthaeus, W. H., Dasso, S., & Kivelson, M. G. 2011, *J. Geophys. Res.*, 116, A08102
- Yang, L., Wang, L., Li, G., et al. 2018, *ApJ*, 853, 89
- Zank, G. P., Li, G., Florinski, V., et al. 2006, *J. Geophys. Res.*, 111, A06108
- Zank, G. P., & Matthaeus, W. H. 1992, *J. Geophys. Res.*, 97, 17189
- Zank, G. P., Rice, W. K. M., & Wu, C. C. 2000, *J. Geophys. Res.*, 105, 25079

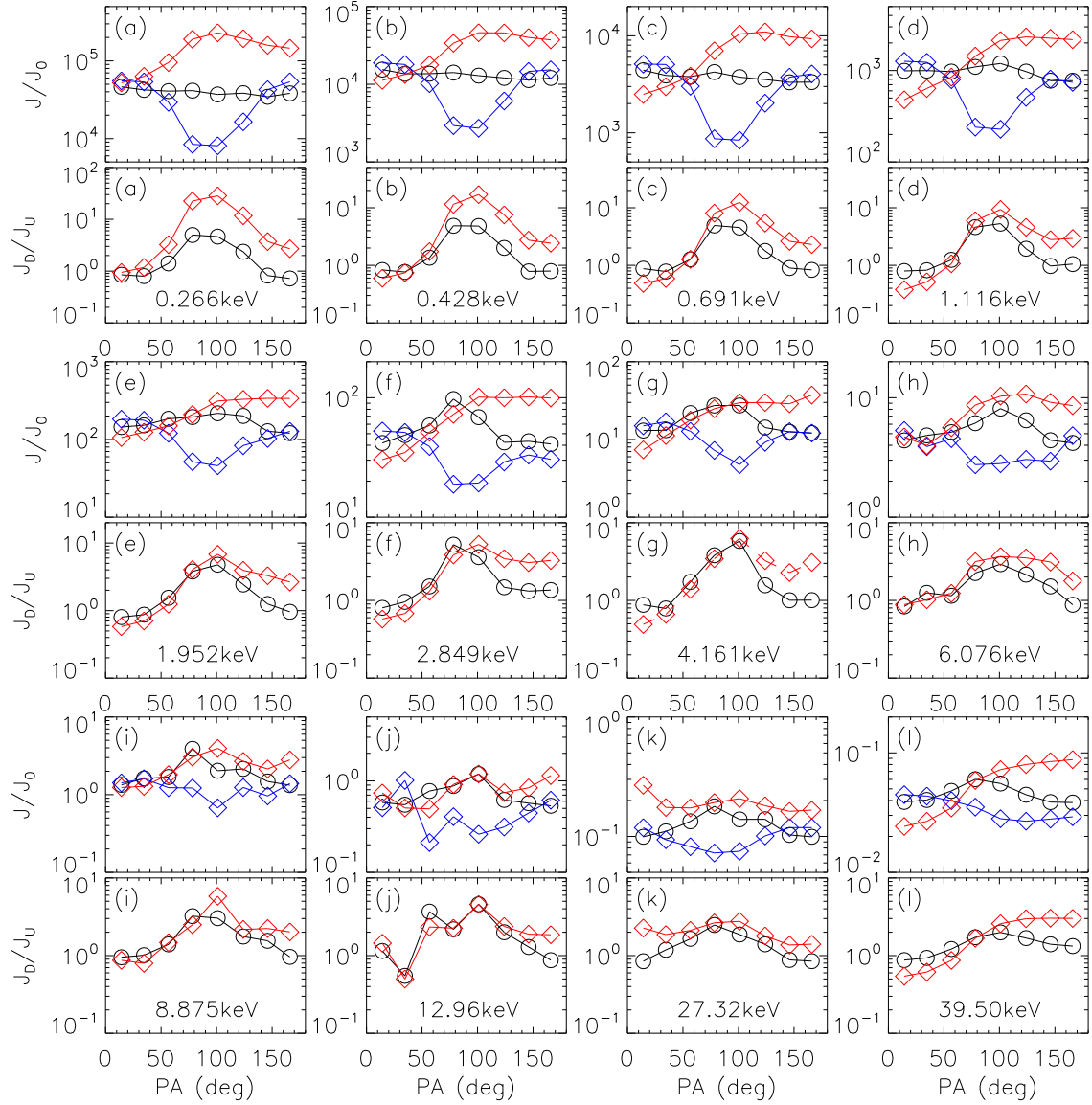


**Figure 1.** Electron differential intensity vs. pitch angle in the energy channels of 0.266–39.50 keV marked with (a)–(l). In the upper panels of the figures (a)–(l), the blue and red diamonds correspond to 10-minute averaged upstream and downstream intensities from observations, respectively, and the black circles are results from simulations using an initial distribution based on the observed upstream intensities. In the lower panels, red diamonds (black circles) show the ratio of the downstream intensities for observations (simulations) to the upstream intensities. Note that  $J_0$  denotes a unit of intensity ( $1 \text{ cm}^{-2} \text{ s}^{-1} \text{ sr}^{-1} \text{ eV}^{-1}$ ).

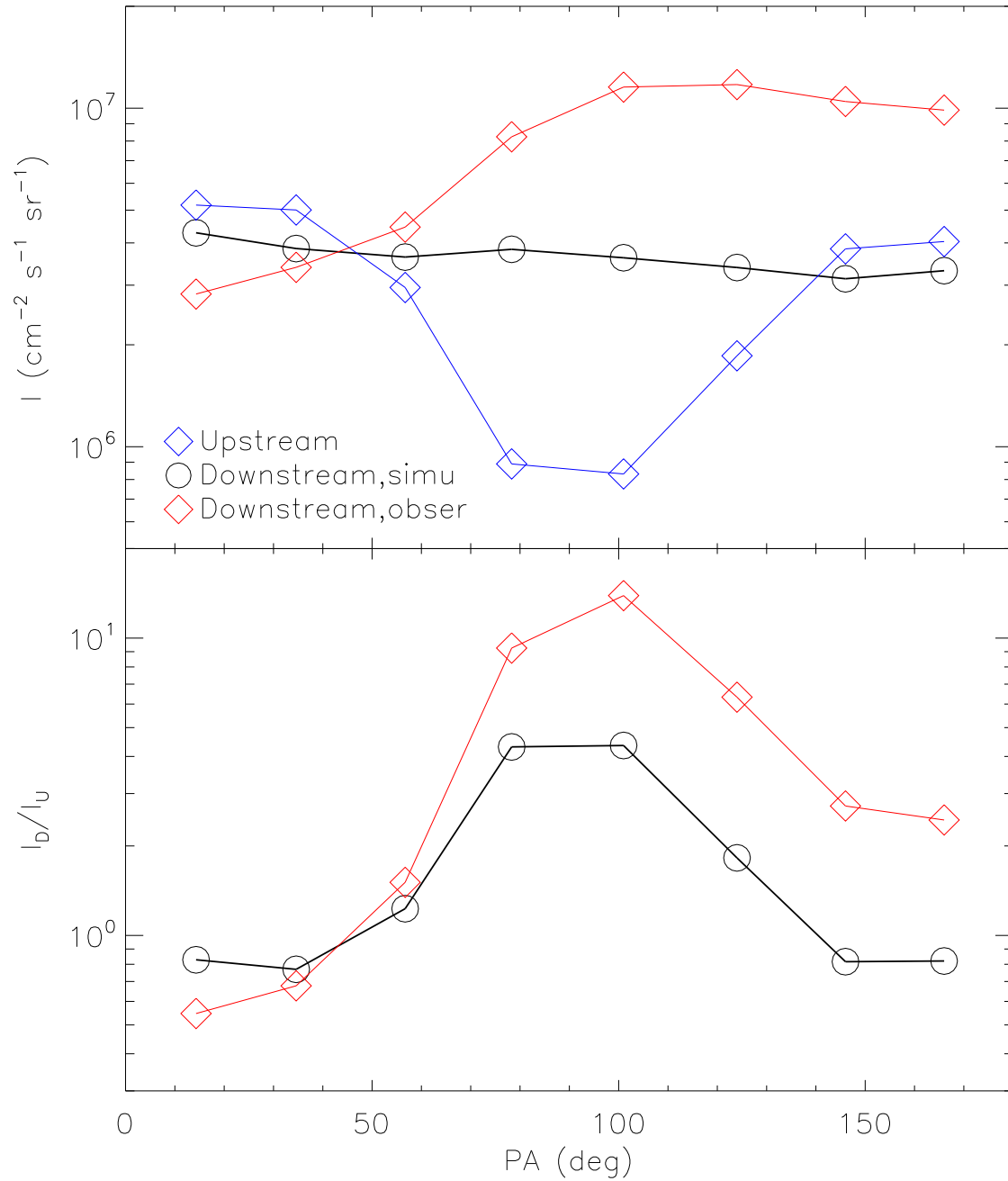


**Figure 2.** Upper panel: Integral over the energy range 0.266–39.50 keV of the differential intensity spectrum in each pitch angle direction for the upstream (blue diamonds), downstream obtained from simulations (black circles), and downstream from observations (red diamonds). Lower panel: Red diamonds (black circles) show the ratio of the downstream integral intensity for observations (simulations) to the upstream intensity.



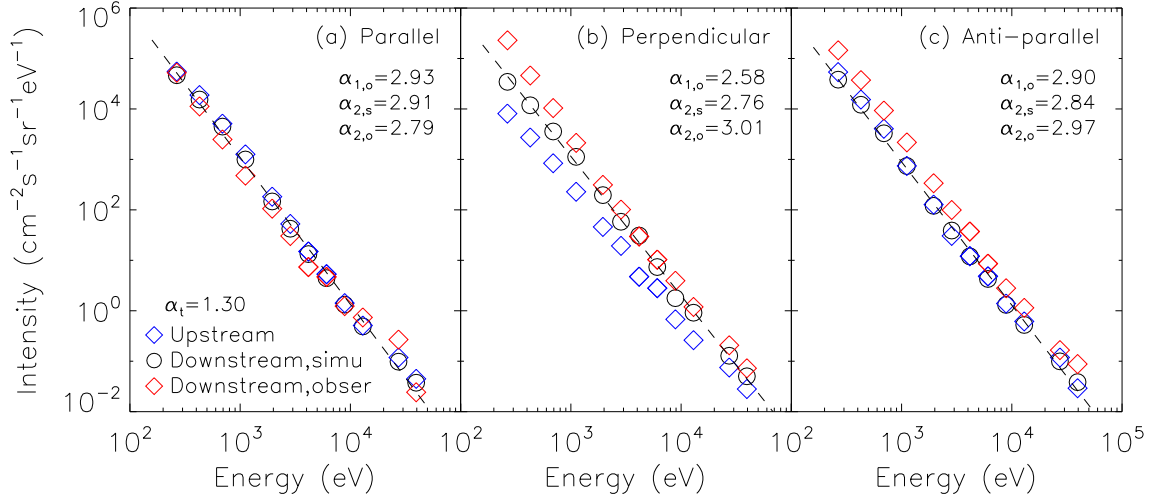


**Figure 3.** Electron energy spectra in the directions parallel (a), perpendicular (b), and anti-parallel (c) to the magnetic field. The blue (red) diamonds denote 10-minute averaged electron intensities in the upstream (downstream) of the shock. The black circles correspond to the downstream intensities obtained from simulations. The values of  $\alpha_{1,o}$ ,  $\alpha_{2,o}$ , and  $\alpha_{2,s}$  correspond to the energy spectral indices of power-law fits to observational data in the upstream and downstream regions, and simulations in the downstream, respectively. Dashed line indicates the power-law fitting of the simulation results in the downstream. Also denoted is the theoretical spectral index,  $\alpha_t$ .

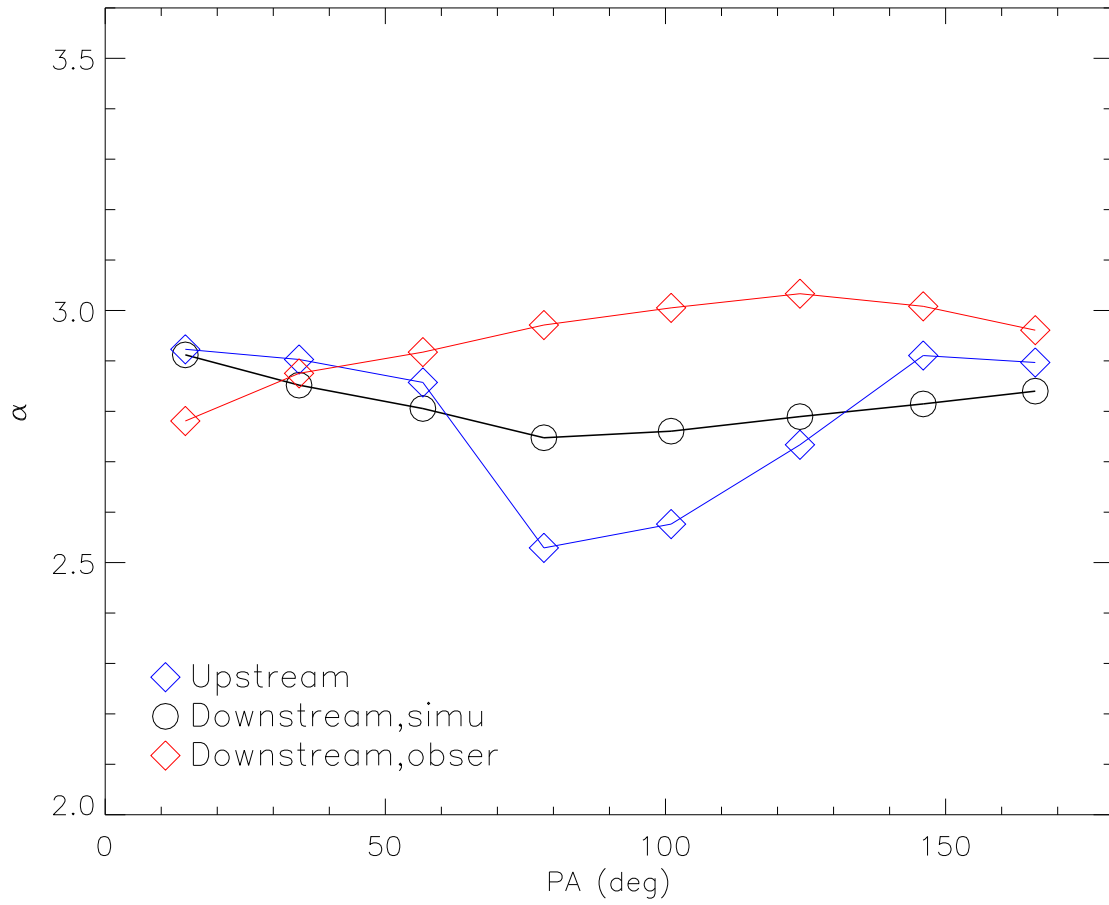


**Figure 4.** Energy spectral index by a power-law fit to the energy spectrum in each pitch angle direction in Figure 1. The blue and red diamonds indicate the results from the observations in the upstream and downstream, respectively. The black circles indicate the results from simulations in the downstream.

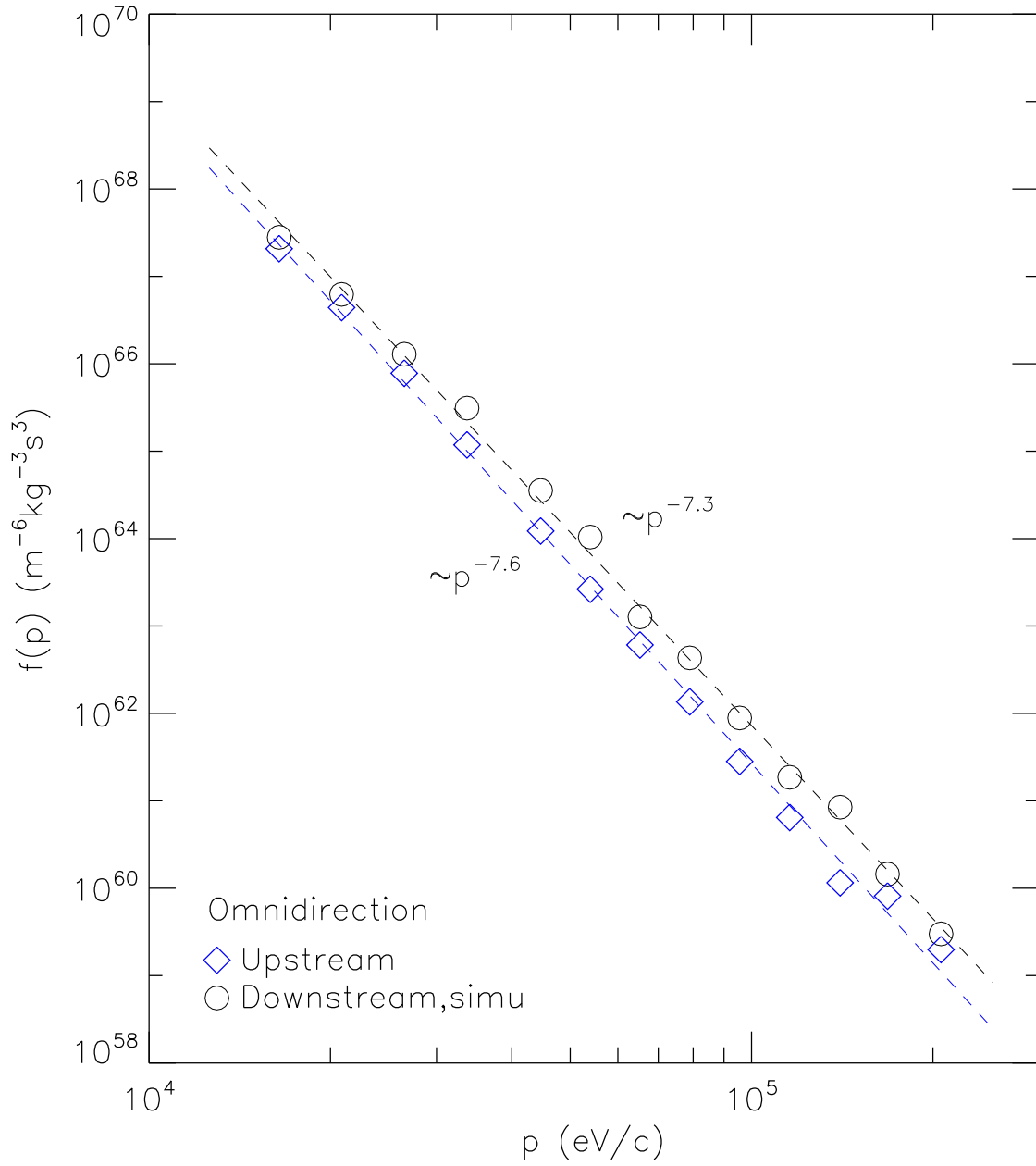


**Figure 5.** Omnidirectional momentum distributions for observations in the upstream (blue diamonds) and simulations in the downstream (black circles), and their power-law fits with dashed lines.

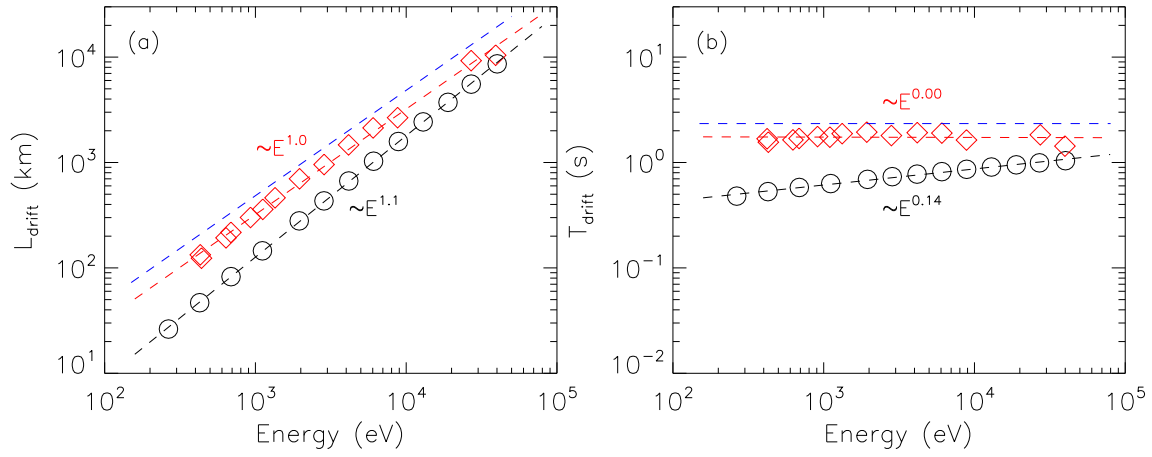


**Figure 6.** The drift length  $L_{\text{drift}}$  and the drift time  $T_{\text{drift}}$  as a function of electron energy in (a) and (b), respectively. Red diamonds and black circles indicate results from observations in YEA2018 and our simulations, respectively. Red and black dashed lines indicate the linear fitting of the data from observations and simulations, respectively. Blue dashed lines indicate the theoretical results.

**Table 1.** Input Parameters for the Shock

Parameter	Description	Value
$\theta_{Bn}$	shock angle	$89^\circ$
$V_{sh}$	shock speed	$682 \text{ km s}^{-1}$
$s$	compression ratio	2.87
$B_{01}$	upstream magnetic field	7.0 nT
$L_{th}$	shock thickness	$2 \times 10^{-6} \text{ AU}$
$U_1$	upstream speed	$248 \text{ km s}^{-1}$
$M_{A1}$	upstream Alfvén Mach number	3.70

**Table 2.** Input Parameters for the Turbulence

Parameter	Description	Value
$\lambda$	slab correlation length	0.02 au
$\lambda_x$	2D correlation length	$\lambda/2.6$
$E_{\text{slab}} : E_{2\text{D}}$	two-component energy density ratio	20 : 80
$(b/B_0)^2_1$	upstream turbulence level	0.25
$(b/B_0)^2_2$	downstream turbulence level	0.36
$k_b$	break wavenumber	$10^{-6}$ m
$\beta_i$	inertial spectral index	5/3
$\beta_d$	dissipation spectral index	2.7